Revision 1

Phase relationships in the system ZnS-CuInS$_2$: insights from a nanoscale study of indium-bearing sphalerite

JING XU[1,2,*], CRISTIANA L. CIOBANU[2], NIGEL J. COOK[2], ASHLEY SLATTERY[3], XIAOFENG LI[1,4,5],
ALKIVIADIS KONTONIKAS-CHAROS[2]

[1]*Key Laboratory of Mineral Resources, Institute of Geology and Geophysics, Chinese Academy of Sciences, Beijing, 100029, China*
[2]*School of Chemical Engineering and Advanced Materials, The University of Adelaide, SA 5005, Australia*
[3]*Adelaide Microscopy, The University of Adelaide, SA 5005, Australia*
[4]*Institutions of Earth Science, Chinese Academy of Sciences, Beijing 100029, China*
[5]*College of Earth and Planetary Sciences, University of Chinese Academy of Sciences, Beijing 100049, China*

ABSTRACT

Micron- to submicron-scale indium-rich domains are preserved within sphalerite included in hornfels-hosted pyrrhotite from the Dulong polymetallic skarn, Yunnan, China. The nano-mineralogy of the ZnS-bearing blebs was investigated using scanning transmission electron microscopy on thinned foils extracted *in-situ* from pyrrhotite. Indium incorporation in sphalerite occurs via the coupled substitution $2Zn^{2+} \leftrightarrow Cu^{+} + In^{3+}$, the results thus allow insights into phase relationships in the system ZnS-CuInS$_2$ in which solubility limits are debated with respect to a cubic to tetragonal phase transition. The highest

---

[*] Corresponding author. e-mail address: xujing3800@126.com; j.xu@adelaide.edu.au

concentrations of In are measured in basket-weave domains from the smallest ZnS blebs or from un-patterned areas in coarser, irregular ZnS inclusions in pyrrhotite. Indium-rich domains contain 17-49 mol.% $CuInS_2$, whereas In-poor sphalerite contains <5 mol.% $CuInS_2$. Atomic-scale metal ordering observed in In-(Cu)-rich ZnS domains was modelled as mixed sites in a cubic structure with $P\bar{4}3m$ symmetry and empirical formula $[(Cu,In,Zn)_3(Zn_{0.5}Fe_{0.5})]_4S_4$. This sphalerite modification is distinct from the cubic-tetragonal phase transition reported elsewhere for analogous, synthetic phases with abundant planar defects. The $Zn_{1.5}Fe_{0.5}CuInS_4$ nanophase described here potentially represents a Fe-bearing polymorph of Zn_2CuInS_4, considered as an endmember in the sakuraiite solid solution series. At $\leq$50 mol.% $CuInS_2$ in the ZnS-$CuInS_2$ system, incorporation of In via coupled In+Cu substitution is promoted within a cubic ZnS phase with lower symmetry than sphalerite rather than into the spatially co-existing chalcopyrite of tetragonal symmetry. Solid state diffusion accounts for phase re-equilibration resulting in the basket-weave textures typical of In-(Cu)-rich domains in the smallest blebs, whereas fluid percolation assists grain coarsening in the irregular inclusions. The results show evidence for existence of more complex phase transition than previously recognized from experimental studies, and intriguingly, also to a potential eutectic in the system ZnS-$CuInS_2$. Pyrrhotite-bearing hornfels in skarns may concentrate In and other critical metals hosted in sphalerite and related sulfides due to the efficient scavenging from fluid by these minerals and the subsequent preservation of those included phases by sealing within the pyrrhotite matrix.

Keywords: Sphalerite, indium, system ZnS-$CuInS_2$, HAADF STEM

INTRODUCTION

Sphalerite is the dominant source of indium (In), a critical element of economic interest due to expanding applications in photoconductors, semi-conductors and other advanced technologies (e.g., Werner et al. 2017). Knowledge about how critical metals occur in nature is of importance for identifying new resources and optimizing recovery from existing operations. This is particularly relevant in the case of In which seldom forms independent minerals.

Zinc sulfide (ZnS) crystallizes as close-packed structures, of which the most common are the cubic 3*C* and hexagonal 2*H* structures in sphalerite, (Zn,Fe)S, and its polymorph wurtzite, respectively (Pósfai and Buseck 1997, and references therein; Table 1). These are referred to as ZnS_{3C} and ZnS_{2H} hereafter. Indium is a chalcophile element, almost exclusively occurring in sulfides (Cook et al. 2011a) and, in most base metal sulfide ores, will be preferentially partitioned into sphalerite over co-existing Cu-Fe-sulfides (George et al. 2016). Unlike isovalent substitutions, e.g., $Zn^{2+} \leftrightarrow Fe^{2+}$, incorporation of trivalent atoms such as In^{3+} requires a coupled substitution, of which the most common is: $2Zn^{2+} \leftrightarrow Cu^{+} + In^{3+}$ (e.g., Cook et al. 2012). Other substitution mechanisms have, however, been proposed based on measured inter-element correlations, including those involving available monovalent ions (e.g., Ag^{1+}), and Sn commonly considered of tetravalent charge. Such substitutions are more complex and stipulate presence of vacancies (□) or different oxidation state for Sn, e.g., $3Zn^{2+} \leftrightarrow In^{3+} + Sn^{3+} + \square$ (Belissont et al. 2014), $3Zn^{2+} \leftrightarrow In^{3+} + (Cu,Ag)^{+} + Sn^{2+}$ (Frenzel et al. 2016), and $4Zn^{2+} \leftrightarrow In^{3+} + Sn^{4+} + (Cu,Ag)^{+} + \square$ (Frenzel et al. 2016).

Conversion between the 3*C* and 2*H* structures, as well as formation of numerous ZnS polytypes, is readily promoted by screw dislocations and twin mechanisms as shown by transmission electron microscopy (TEM) and X-ray diffraction (e.g., Akizuki 1981; Fleet 1977). Phase transformations between ZnS species and substitution mechanisms can be accommodated by polysynthetic twinning along <111> planes in 3*C* ZnS, as documented by TEM studies of Fe-rich, Ge-(Fe)-rich, In-Cu-(Fe)-bearing sphalerite, and analogous ZnS-derived compounds (e.g., Pósfai et al. 1988; Bente et al. 1998; Wagner et al. 2000a, b; Šrot et al. 2003; Ciobanu et al. 2011; Cook et al. 2015).

Studies of the system ZnS-$CuInS_2$ (Sombuthawee et al. 1978; Schorr et al. 2004) show extensive solubility but incomplete solid solution due to structural transition between cubic ZnS and the tetragonal (chalcopyrite-type) structure of $CuInS_2$ (roquesite). Schorr and Wagner (2005) observed a miscibility gap between ~40 and ~90 mol.% $CuInS_2$ based upon a neutron diffraction study of metal ordering in the solid solution $2ZnS$-$CuInS_2$. Nonetheless, complete solid solution in the system ZnS-$CuInS_2$ is supported by TEM studies of $Zn_{2-2x}Cu_xIn_xS_2$ (ZCIS; $0.78<x<1$) alloys showing that the transition between tetragonal chalcopyrite-type ($x>0.78$) and cubic sphalerite-type ZCIS ($x<0.78$) is accommodated by formation of twinned nanodomains with 'CuAu-I' type ordering (Wagner et al. 2000a). *Ab initio* calculations and synthesis of $CuInS_2$ alloys with non-chalcopyrite ordering show that the Cu^{1+} and In^{3+} atoms are placed on alternating (100) planes ('CuAu-I' type substitution) rather than at (201) planes (chalcopyrite-type substitution) in the ZnS_{3C} structure, leading to compounds with $P\bar{4}m2$ symmetry (Wei et al. 1992; Su et al. 1998). Metastable phases with 'CuAu-I' ordering occur spontaneously in the systems ZnS-$CuInX_2$ (X=S, Se) during polymorphic transition between ZnS_{3C} and chalcopyrite-type compounds at temperatures in the range 800-1300 K (Wei et al. 1992, and references therein).

Advances in electron microscopy techniques, and particularly Z-contrast imaging using high-angle annular dark field scanning transmission electron microscopy (HAADF STEM) on thinned foils extracted *in-situ* from samples previously characterized with respect to composition, allows unparalleled insights into crystal-chemistry and metal ordering in ore minerals at the nanoscale (Ciobanu et al. 2016a).

Understanding of the crystal-structures of In-bearing ZnS and related phases draws largely on the results of investigation of synthetic samples and remains largely unstudied in natural materials. Although In-bearing sphalerite has been reported from a variety of polymetallic ores, occurrences lacking other sulfides into which the same trace elements may partition, are rare. The present HAADF STEM study is carried out on In-rich sphalerite occurring as inclusions within pyrrhotite, a matrix in which In is incompatible, thus offering an excellent opportunity to assess phase transitions among natural phases in the system ZnS-$CuInS_2$. This material derives from the In-bearing Dulong Sn-polymetallic skarn deposit, Yunnan Province, China (Xu et al. 2020). In this contribution, we aim to assess (i) In-distribution and concentration in sphalerite inclusions with various textures, and (ii) identify metal order or disorder throughout In-rich domains.

BACKGROUND: SPHALERITE AND RELATED SULFIDE GROUPS

The debate surrounding crystal chemistry of species within the system Zn-Cu-In-Sn-Fe-S is useful in understanding phase transition from cubic to tetragonal and vice versa between related sulfide groups. Microanalysis of natural sphalerites have shown that In concentrations can extend up to wt.% levels (e.g., Cook et al. 2009 and references therein). There are, however, In-bearing, ZnS-related sulfides, i.e., sakuraiite and ishiharaite (Table 1), in which the sum of substituting metals can make up to 80-90 wt.%. Whereas ishiharaite (Cu,Ga,Fe,In,Zn)S was defined as a $F\bar{4}3m$ sphalerite-type structure in which all metals are placed in a single crystallographic site (Márquez-Zavalía et al. 2014), the crystal chemistry of sakuraiite is still open to debate (see discussion in Momma et al. 2017). Sakuraiite was reported either as $(Cu,Zn,Fe)_3(In,Sn)S_4$, as tetragonal phase with extended In for Sn substitution (Kato 1965; Shimizu et al., 1986; Momma et al. 2017), or cubic (Cu,Zn,In,Fe,Sn)S, with three possible space groups suggested ($P432$; $P\bar{4}3m$ and $Pm3m$; Kissin and Owens 1986) (Table 1).

A parallel can be drawn to the related stannite group whereby the join between stannite and kësterite, Cu_2FeSnS_4 – Cu_2ZnSnS_4 (Table 1) has also been subject to much debate in terms of continuous or discontinuous solid solution, phase stability and crystal structures (Table 1; Bonazzi et al. 2003, and references therein). The Cu_2FeSnS_4 phase had been considered as the mineral isostannite but was formally discredited (Kissin and Owens 1989), based on new analysis of type material, which was found to consist of stannite and kësterite. Kissin and Owens (1989) noted, however, that the study of type material did not preclude the potential existence of a cubic polymorph of stannite.

Two models, with different distribution of cations among positions at (0,0,0), (0,½,¼) and (0,½,¾) coordinates, have been proposed for structurally-related yet nevertheless distinct minerals, i.e., $I\bar{4}2m$ and $I\bar{4}$ space groups for stannite and kësterite, respectively (Hall et al. 1978). These were later re-evaluated within a single, higher symmetry $I\bar{4}2m$ structural model but with distinct cation occupancies for the two endmember minerals (Bonazzi et al. 2003). A cubic modification of stannite, $Cu_{2-x}Fe_{1-x}SnS_4$, was identified by Rietveld methods as a ZnS-derivative with lower symmetry ($P\bar{4}3m$; Table 1) and this is characterized by mixed sites comprising Sn + Fe (position 1a: 0,0,0) and Cu + Fe + Sn (position 3c: 0,1/2,1/2) (Evstigneeva and Kabalov 2001). This phase is likely the same phase synthesized earlier by Springer (1972). Re-examination of Springer's experimental products and Guinier films (Kissin 1989) confirmed the presence of such a phase. Kissin and Owens (1979) and Kissin (1989) showed, however, that end-member stannite and kësterite are synthesized at 800 °C. One might therefore conclude that if a high-temperature, cubic polymorph of stannite exists, it must be unquenchable and that different synthetic products may be obtained depending on temperature and annealing steps during cooling, consistent with the conclusion of Kissin (1989) that at lower temperature conditions, Fe-rich compositions do not yield equilibrium stannite structures and compositions. In a subsequent publication, Evstigneeva et al. (2001) discussed a larger stannite family based on Cu-Fe isomorphism in these sulfides.

The latest reinvestigation of sakuraiite type material by single crystal X-Ray diffraction led to a pseudo-tetragonal phase ($P4\bar{}2m$) considered as an intermediate member of the stannite-Zn_2CuInS_4 solid solution (Momma et al. 2017). These authors distinguished between Cu, Zn and Fe atoms randomly distributed in two crystallographic sites (1a and 2f) and Sn which is placed in a distinct site (1d), concluding that this type of metal ordering is different from that of other known sulfides, e.g., sphalerite ($F\bar{4}3m$), stannite ($I\bar{4}2m$), kësterite ($I\bar{4}2m$ or $I\bar{4}$) and chalcopyrite ($I\bar{4}2d$) (Momma et al. 2017).

The complexity of phases in the Zn–Cu–(Ag)–(Fe)–(In)–Sn–S system is further emphasized by the variety of minerals that have chalcopyrite- or stannite-like structures (Table 1). Some of these have been reported as nanoparticles (NPs) within sphalerite (e.g., Ciobanu et al. 2011) or have been synthetized as multi-component $(ZnS)_x(Cu_2SnS_3)_{1-x}$ and $(CuInS_2)_x(Cu_2SnS_3)_{1-x}$ nanocrystals with metastable ZnS structures (e.g., Liu et al. 2011).

SAMPLES AND METHODOLOGY

The sample of pyrrhotite-bearing hornfels (biotite schist) contains some of the In-richest sphalerite in the Dulong deposit (In contents between 0.21 and 14.75 wt.% based on EPMA data; Xu et al. 2020). Five thin foils for nanoscale study (Supplemental[1] Fig. S1) were prepared using focused ion beam (FIB)-SEM by cutting across sphalerite blebs or boundaries to pyrrhotite (Fig. 1). Each foil was placed on a copper grid and thinned.

HAADF STEM imaging was performed using an ultra-high resolution, probe-corrected, FEI Titan Themis S/TEM. This instrument is equipped with the X-FEG Schottky source and Super-X EDS geometry. The Super-X EDS detector provides geometrically symmetric EDS detection with an effective solid angle of 0.8 Sr. Probe correction delivered sub-Ångstrom spatial resolution and an inner collection angle greater than 50 mrad was used for HAADF experiments using the Fischione HAADF detector. Diffraction measurements were performed using DigitalMicrograph™ 3.11.1 and Winwulff© 1.4.0 software. Data from the American Mineralogist Crystal Structure Database were used for indexing of the electron diffractions. Crystal structure simulations were carried out using CrystalMaker® version 9.2.7 and STEM™ for xHREM software.

---

[1] Deposit Item

RESULTS

Micron to nanoscale textures and indium distribution in sphalerite

The studied sphalerite occurs as irregular, bleb-like, or lobate inclusions in pyrrhotite (Fig. 1). On the surface of the polished block, In-rich areas have patchy distribution within the irregular, coarser sphalerite inclusions (Fig. 1a, b) or make up the larger part of the smaller sphalerite blebs (Fig. 1c, d). Single grains of pyrrhotite can also occur within the coarser lobate sphalerite (Fig. 1e). The FIB cuts were placed across all three types of textures exposing the sphalerite inclusions at depth, as well as phase boundaries and the presence of chalcopyrite and other mineral NPs, particularly Bi-(Ag)-phases (Fig. 2).

HAADF STEM imaging shows In-rich and -poor domains with scalloped or concave mutual boundaries (Fig. 2a, b) and the presence of phyllosilicates that crosscut the sphalerite blebs (Fig. 2c). Nanometer-wide fractures are marked by the presence of chalcopyrite NPs, often along sets of trails (Fig. 2d). Relative enrichment in indium occurs along some mutual boundaries between sphalerite and pyrrhotite (Fig. 2e). In contrast, the In-rich domains in the sphalerite blebs display a basket-weave texture formed by nm-wide lamellae of In-poor sphalerite (Fig. 2f). In detail, the boundaries between In-rich and -poor domains from the coarser inclusions are very irregular whereas those between sphalerite and pyrrhotite are sharp (Fig. 2g). Similar enrichment in In is also observed surrounding NPs of native bismuth (Fig. 2h). Some of the domains richest in In tend to develop a euhedral morphology, e.g. as hexagonal platelets (Fig. 2i). Chalcopyrite NPs along fractures in the lobate sphalerite display euhedral to sub-rounded morphology (Fig. 2j). The margins between the sphalerite in pyrrhotite are marked by enrichment in Bi and Ag and by formation of discrete NPs of Bi-Ag-bearing minerals (possibly sulfosalts; Fig. 2k). Other fractures, no more than a few nm in width, are marked by enrichment in Cu, Si, and O (Supplemental[1] Fig. S2a, b).

EDS-STEM mapping and spot analysis shows further details of the distribution of In and other trace elements in sphalerite (Figs. 3-6; Supplemental[1] Figs. S2, 3). Indium is present along the entire length of the sphalerite inclusion exposed at depth in foil #1, albeit with a patchy, irregular distribution (Fig. 3a). EDS maps at higher resolution show that In concentrations correlate positively with Cu (Fig. 3b). Notably, chalcopyrite inclusions within the same area display no In-content (Fig. 3c), whereas the correlation between Cu and In is clearest in sphalerite from an adjacent domain in the same area (Fig. 3d). The assemblage also includes NPs of native copper, observed within both chalcopyrite and sphalerite (Fig. 3c, e).

Maps of the sub-rounded sphalerite inclusion in pyrrhotite from foil #2 (Fig. 4) display conspicuous In-enrichment around NPs of native bismuth and also around boundaries to adjacent pyrrhotite (Fig. 4b, c). The illustrated inclusion is crosscut and displaced by lamellae of phyllosilicates, most likely an intergrowth of chlorite and phlogopite (Supplemental[1] Fig. S3). The smallest sphalerite blebs in pyrrhotite show In-enrichment in the domain with basket-weave texture (foil#3; Fig. 5a). In both the irregular and bleb-like sub-types of sphalerite inclusions in pyrrhotite, Fe is concentrated within the In-rich domains rather than in the In-poor sphalerite (Figs. 3d and 5a). Chalcopyrite NPs mapped from trails within sphalerite (Fig. 5b, Supplemental[1] Fig. S2c, d) show negligible In content.

Representative EDS spectra for sphalerite, chalcopyrite and various NPs are shown in Supplemental[1] Figure S4. Sphalerite from In-rich areas in different foils/textures show comparable Fe to In ratios (spectra #2-5; 7 shown on Supplemental[1] Figure S4). Spectra obtained from adjacent In-poor sphalerite still show the presence of Fe and minor In (spectra #1 and 6 on Supplemental[1] Figure S4). The lobate sphalerite from foil #5 shows Fe at comparable concentration with the other areas but the lowest content of In (spectrum #8 in Supplemental[1] Figure S4). Chalcopyrite from the irregular sphalerite (Fig. 3c) differs from the chalcopyrite along trails in lobate sphalerite (Fig. 5b) in that it contains measurable Zn. Neither contain other minor/trace elements at concentration levels measurable by EDS STEM analysis (spectra #9 and 10 in Supplemental[1] Figure S4). The 'trail chalcopyrite', however, hosts Ag- and Ag-Bi-bearing NPs, comparable to those present along margins between sphalerite and pyrrhotite in the same sample (foil#5; spectra #11-13 in Supplemental[1] Figure S4).

EDS spot analyses obtained from the mapped areas (Table 2; Supplemental[1] Table S1) have been plotted in terms of mol.% $CuInS_2$ versus lattice parameter using data given by Wagner et al. (2000) (Fig. 6). Since very small volumes were analyzed without use of standards, these data must be considered semi-quantitative. Mol.% $CuInS_2$ was calculated by assigning equal atom% Cu as In (to correct for overreading of Cu from the grid) and normalizing to 100%; Fe content was added to Zn. The plot shows a compositional spread for In-rich sphalerite between 17-49 mol.% $CuInS_2$, whereas In-poor sphalerite contains <5 mol.% $CuInS_2$.

High-resolution imaging – defects and phase transformation

In order to assess the identity of substituted ZnS phases mapped as inclusions in pyrrhotite, high-resolution HAADF STEM imaging of the five foils was undertaken by tilting the specimen up to four main zone axes in each area or sample. Fast Fourier transform (FFT) patterns obtained from images were indexed, and STEM simulations on these orientations show a good match with the images and crystal structure models (Fig. 7). Simulations undertaken for roquesite as an analog for a tetrahedral structure (Supplemental[1] Fig. S5) show similar patterns as cubic ZnS on the [001] zone axis but distinct 'dumbbell' In and Cu atom pairs for the [100], [101], [111] and $[1\bar{2}1]$ zone axes. Such 'dumbbell' patterns were however observed only across small strips at phase boundaries between In-rich and -poor areas (see below).

Simple stacking faults occur as stepwise defects along {111} directions (Fig. 8a), but the continuity of the atomic arrays across the boundaries between In-poor and -rich domains, is generally preserved in all inclusion types (Fig. 8b, c). Nonetheless, In-rich sphalerite at the boundary with native bismuth displays quasi-regular cation ordering expressed as alternating brighter and dimmer atoms along *b* and *c* axes (Fig. 8d, e; see also below).

In further detail, the {111} defects are associated with lattice distortion leading to irregular atom displacements (Fig. 9a-f). These defects can form a regular network defining euhedral shapes (Fig. 9a), resembling those shown for In-rich areas on Figures 2i and 3d. More often, however, these defects form a zig-zag pattern and their length is less than 50 nm (Fig. 9b). In either case the FFT patterns on the $[0\bar{1}1]$ zone axis show disorder on <111>* lattice vectors rather than twinning (Fig. 9c). Atom arrangements change along the stacking faults from simple kinks to several dumbbell arrays (Fig. 9d-f). Screw dislocations along {111} fault planes are associated with variable width and atomic disorder (Fig. 9g). Structural disorder is also observed as local defects shown as spotted darker areas on $[1\bar{1}1]$ (Fig. 9h). In detail, such areas are associated with a decrease in total signal intensity, suggesting the presence of atom vacancies (Fig. 9i).

Locally, a transformation from [100]-cubic ZnS to [100]-tetragonal roquesite-type is observed along 10-20 nm-wide stripe at the In-enriched boundary between sphalerite and pyrrhotite (foil #2; Fig. 10a). In contrast, preservation of the [100] cubic ZnS structure across boundaries of In-enrichment is associated with quasi-regular ordering of brighter/larger atoms as a ~5Å x 5Å pattern, which is easy to visualize at the direct contact to ZnS_{3C} (Fig. 10b). The FFT pattern (inset, Fig. 10b) shows the structure with quasi-ordering of brighter atoms within the ZnS substructure. In closer detail, the roquesite-type pattern displays a dumbbell atomic arrangement with satellite reflections at ½ <011>* (Fig. 10c, d). This is different from the square, ~5Å x 5Å, pattern formed by brighter atoms attributable to columns of In-(Cu, Zn) mixed sites (Fig. 10e). Corresponding FFT pattern is distinct from the one shown as Figure 10d in that it features additional satellite reflections along b^* and c^*, which are forbidden for the space group $F\bar{4}3m$ of ZnS_{3C} (compare Fig. 10f with Fig. 7a). The HAADF STEM image and FFT for this type of ZnS transformation are also distinct from the [001] roquesite-type structure (Supplemental[1] Fig. S5).

Pyrrhotite (Supplemental[1] Fig. S6) and sphalerite are not observed to be in epitaxial relationship in any of the samples. Selected area of electron diffraction (SAED) obtained from pyrrhotite images as in Supplemental[1] Figure S6 were indexed using the monoclinic Fe_7S_8 polytype with $C2/c$ space group of Powell et al. (2004) (Supplemental[1] Fig. S6). In detail, the satellite reflections that express metal vacancy ordering are faint and comparable with those known for 1C-type pyrrhotite (Posfai et al. 2000).

DISCUSSION

Trace element incorporation and defects

The studied In-rich ZnS from Dulong is one among many natural specimens showing enrichment in In and other accompanying elements via metal substitution for Zn (Fig. 11). For example, compositionally towards the ZnS end of the ZnS-$CuInS_2$ join is the exceptional In-bearing sphalerite from Toyoha (Japan) sphalerite, which displays exceptional complexity of micron-scale growth rhythms with respect to In and Cu (Cook et al. 2009; Ciobanu et al. 2011; Shimizu and Morishita 2012). Increased structural complexity, polytypism and planar defects such as twins are associated with oscillatory zoning patterns and extend down to the nanoscale (Ciobanu et al. 2011), yet crystal-structural continuity across In-poor and In-rich boundaries is recognized, as indicated by HAADF STEM imaging (Ciobanu et al. 2016b). This observation implies random metal substitution on a single site, thus preserving the cubic sphalerite symmetry, as in the high-substituted ZnS structure of ishiharaite (Márquez-Zavalía et al. 2014).

Assessment of HAADF STEM images, as well as FFT patterns produced by defects, is necessary to better constrain the changes within domains with distinct patterns of metal ordering. Although the In-bearing sphalerite from Dulong lacks any chemical zoning or abundant planar defects, the latter, where present (Fig. 9a-g), clearly support formation of high-In domains in the sphalerite. Transition between ZnS_{3C} and tetragonal roquesite-type ($I\bar{4}2m$ space group) structures is limited to such narrow defects (Fig. 10a, c).

Evidence for more complex In substitution mechanisms could be associated with the presence of localized defects (Fig. 9h, i), in which metal loss can be attributed to vacancies, as, for example, those suggested for Sn incorporation into ZnS (e.g., Frenzel et al. 2016). Although Sn concentrations are below the detection limit of the STEM EDX detectors, it is likely this element, otherwise abundant in the Dulong deposit (Xu et al., 2020) is also present in the In-rich ZnS phase at concentrations of least some to tens of ppm.

Cubic modification of In-bearing ZnS: isomorphism and polymorphism in the system Zn-Cu-In-Sn-Fe

The In-rich ZnS from Dulong (up to ~50 mol.% $CuInS_2$; Fig. 6) that displays metal ordering shows FFT patterns comparable with electron diffractions calculated for tetragonal $Zn_{2-2x}Cu_xIn_xS_2$ (ZCIS; $0.78<x<1$) alloys but with numerous nanotwins viewed on [001] direction (Wagner et al. 2000b). However, the ½ *c** and ½ *b** satellite reflections observed in the present study (Fig. 10f) cannot be attributed to twins and their superpositions, as had been discussed for the alloys, since such planar defects are not present (HAADF STEM images shown as Figs. 8c and 10b). The HAADF STEM images and corresponding FFT patterns can be simulated if we consider a model comparable to the cubic modification of the Cu_2FeSnS_4 compound reported by Evstigneeva and Kabalov (2001). In our case, the In-rich ZnS with $P\bar{4}3m$ symmetry and empirical formula $[(Cu,In,Zn)_3(Zn_{0.5}Fe_{0.5})]_4S_4$ was modelled as a phase with two mixed sites: Me1a (In, Cu, and Zn); and Me3c (Zn and Fe) (Fig. 12a). The simulated electron diffraction and STEM images (Fig. 12b, c) show a good fit with the measured FFT patterns and HAADF STEM images (Fig. 10e, f). HAADF signal intensity profiles obtained across selected directions in the In-rich ZnS displaying metal ordering show variation, as predicted by the proposed crystal model (Fig. 12d, e). Importantly, these profiles are distinct from those recorded in adjacent In-poor ZnS (Fig. 12f, g).

As a result, we conclude that partial metal ordering occurring in the In-rich ZnS from Dulong represents a cubic modification of sphalerite that is distinct from the cubic-tetragonal phase transition reported for ZCIS compounds (Fig. 6). The nanophase described here could be considered as a Fe-bearing cubic polymorph of endmember Zn_2CuInS_4 in the sakuraiite solid solution series (Shimizu et al. 1986; Momma et al. 2017), assuming the latter is proven to have tetragonal symmetry. Isomorphism between the synthetic cubic modification of the Cu_2FeSnS_4 phase (Evstigneeva and Kabalov 2001) and $Zn_{1.5}Fe_{0.5}CuInS_4$ (the In-rich ZnS phase from Dulong) extends the 'larger stannite family' of Evstigneeva et al. (2001) to the sphalerite-related structures. The [Cu,Sn] for [(Zn,Fe)In] substitution discussed for sakuraiite-kësterite-stannite along the trend of In/(In+Sn) in phases shown on the Cu-Fe-Zn plot obtained for assemblages from Ikuno Mine, Japan (Shimizu et al. 1986; Momma et al. 2017), may be only one tie-line among several others expressing co-crystallization of phases at specific conditions and not a generic trend.

Formation of In-bearing sphalerite in the Dulong skarn

The diversity of textures involving sphalerite present in the Dulong samples can be interpreted in terms of evolving In-bearing mineral speciation derived from the same early, prograde fluid interacting with host pyrrhotite, via solid state mineral re-equilibration in the smallest blebs to fluid percolation becoming more substantial from the irregular to the larger, lobate sphalerite (Fig. 1). The basket-weave textures observed for the smallest In-rich blebs (Figs. 1c, 2f, and 5a) are comparable to those obtained for the pseudo-binary system 2(ZnTe)-$CuInTe_2$ (Roussak et al. 2005), where they were attributed to sub-solidus transition from cubic to tetragonal symmetry with cation type ordering of a CuPt-type structure. In the studied samples, cubic to tetragonal transition (roquesite-type) is observed only in the larger, irregular inclusions. The coexistence of sphalerite, containing low levels of In, and near endmember roquesite is observed wherever bulk Zn/In ratios in the assemblage are low (e.g., Cook et al. 2011b), and may be indicative of either non-ideal solid solution or the impact of superimposed diffusion-driven processes.

The basket-weave textures are directly attributable to solid state diffusion during which phase re-equilibration takes place, but the curvilinear boundary between In-rich and -poor domains in the blebs (Fig. 2b) more likely represents an initial unmixing or phase-separation corresponding to a binary eutectic at ca. 50 mol. % $CuInS_2$ in the system Zn-Cu-In-S (if Fe is ignored).

The irregular, coarser inclusions with In-bearing sphalerite show more varied chemistry, with nucleation of Cu-, and Bi-, or Bi-Ag-NPs either within chalcopyrite inclusions or along grain boundaries with host pyrrhotite (Figs. 3-5). Coarsening of blebs to irregular inclusions predates formation of phyllosilicates given the crosscutting relationships illustrated in Fig. 4a, indicating that precipitation from In-bearing fluids must have been prior to such retrograde skarn alteration. This episode must nonetheless have followed pyrrhotite formation considering the lack of coherent intergrowths with sphalerite.

The low concentrations of In in the lobate sphalerite indicates that formation of larger pockets of base metal mineralization (Fig. 1e) effectively dilute rather than concentrate In within sphalerite. The tendency for In to be preferentially incorporated into sphalerite over coexisting chalcopyrite at equilibrium (George et al. 2016) is demonstrated here down to the nanoscale (Fig. 5b). The concentration of Cu within In-rich ZnS rather than in the adjacent chalcopyrite NPs is an important observation, in that it corroborates the partitioning of In and Cu into cubic ZnS relative to tetragonal $CuFeS_2$. This is assuming, however, that the chalcopyrite NPs form from locally-generated concentrations of Cu-Fe-rich fluid source, or they post-date initial crystallisation of the In-Cu-Fe-bearing ZnS phase. This shows that the cubic to tetragonal transition in the system ZnS-$CuInS_2$ is not as easy to constrain from natural assemblages, which inherently include Fe, among other cations that could play a role in phase stability and solid-state diffusion responsible for metal ordering.

The presence of Ag- and Bi-NPs indicates, however, a comparable fluid signature with that which precipitated the highest In-sphalerite, thus indicating a continuous mineralizing process rather than discrete stages each featuring distinct fluids. Since bismuth is not easily incorporated into sphalerite, the bismuth NPs provide a diffusion barrier for In-enrichment in ZnS at the contact to such NPs (Fig. 4a, b). Moreover, this barrier also allows for metal ordering leading to the cubic In-rich ZnS with mixed ordering on tetrahedral sites (Figs. 8d and 10b).

IMPLICATIONS

The concentration of In in the initial skarn stage at Dulong is probably not higher than in many other skarn systems, but the retention of unusually high concentrations in early sphalerite relative to later, Sn-rich, base metal sulfide assemblages can be attributed to locking within the pyrrhotite matrix.

Pyrrhotite-bearing hornfels associated with polymetallic skarns may thus represent a critical minerals target. Recent studies have shown enrichment of In, among other critical metals, in basaltic lava (Greaney et al. 2017), the same concept could potentially be applied to pyrrhotite from igneous mafic rocks, in which ZnS and related sulfides would act as scavengers for critical metals from the melt.

Nanoscale studies of natural sphalerite have a critical role to play in gaining a better understanding of the mechanisms of minor element incorporation in sulfides. The research described here also represents a contribution on the fundamental character of solid solution series in common minerals such as sphalerite and related sulfides.

CONCLUDING REMARKS

1. High-In sphalerite (17-49 mol.% $CuInS_2$) is preserved as micron- to submicron-sized areas within ZnS blebs and irregular inclusions in a hornfels-hosted pyrrhotite matrix. Since the incorporation of In within ZnS is coupled with Cu, nanomineralogy of ZnS-bearing assemblages allows insights into phase relationships in the system ZnS-$CuInS_2$.
2. HAADF STEM imaging of In-rich ZnS domains shows metal ordering modelled as mixed sites in a sphalerite-type structure with $P\bar{4}3m$ symmetry and empirical formula $[(Cu,In,Zn)_3(Zn_{0.5}Fe_{0.5})]_4S_4$. This cubic modification of sphalerite is distinct from the cubic-tetragonal phase transition reported for analogous, synthetic phases elsewhere.
3. The $Zn_{1.5}Fe_{0.5}CuInS_4$ nanophase is isomorphous with the cubic modification of Cu_2FeSnS_4 and potentially represents a Fe-bearing polymorph of Zn_2CuInS_4, considered as an endmember in the sakuraiite solid solution series.
4. Indium enrichment, including transformation between [100]-cubic ZnS to [100]-tetragonal roquesite-type structure, is only promoted locally along planar defects (stacking faults and screw dislocations along {111}).
5. Indium concentration in Cu-bearing ZnS domains rather than in adjacent chalcopyrite NPs corroborates partitioning of In and Cu into cubic ZnS relative to tetragonal $CuFeS_2$.
6. Comparable degrees of In-enrichment in sphalerite are achieved during (i) phase separation/unmixing of In-(Cu)-rich domains in ZnS in the smallest, micron-sized In-Cu-Zn-S-bearing blebs with curved domain boundaries; and (ii) fluid percolation resulting in bleb-coarsening and irregular morphology. Solid-state diffusion accounts for phase re-equilibration in the basket-weave texture typical of In-(Cu)-rich domains in the smallest blebs. Metal ordering, leading to the cubic In-rich ZnS with mixed ordering on tetrahedral sites, is assisted by the presence of diffusion

barriers such as Bi-NPs in the coarsest irregular blebs. An increase in fluid/rock ratio dissipates In within the largest, lobate sphalerite containing the lowest content of this element.

7. Pyrrhotite-bearing hornfels in a skarn deposit is a potential host for In and other critical metals hosted in sphalerite and related sulfides due to efficient scavenging from fluid by these minerals and subsequent locking within the pyrrhotite matrix.

ACKNOWLEDGEMENTS

This work was carried out while J.X. was a visitor at the University of Adelaide. Funding from the National Key RandD Program of China (2017YFC0602500), Key Laboratory of Mineral Resources (KLMR2017-13), China Postdoctoral Science Foundation, and the China Scholarship Council. We gratefully acknowledge Microscopy Australia for access to instrumentation. We acknowledge insightful comments two *American Mineralogist* reviewers, Associate Editor Daniel Harlov, as well as comments from two reviewers of an earlier version of this manuscript.

REFERENCES

Abrahams, S.C., and Bernstein, J.L. (1973) Piezoelectric nonlinear optic $CuGaS_2$ and $CuInS_2$ crystal structure: Sublattice distortion in $A^{I}B^{III}C_2^{VI}$ and $A^{II}B^{IV}C_2^{V}$ type chalcopyrites. Journal of Chemical Physics, 59, 5415-5420.

Akizuki, M. (1981) Investigation of phase transition of natural ZnS minerals by high resolution electron microscopy. American Mineralogist, 66, 1006-1012.

Belissont, R., Boiron, M.C., Luais, B., and Cathelineau, M. (2014) LA-ICP-MS analyses of minor and trace elements and bulk Ge isotopes in zoned Ge-rich sphalerites from the Noailhac–Saint-Salvy deposit (France): Insights into incorporation mechanisms and ore deposition processes. Geochimica et Cosmochimica Acta, 126, 518-540.

Bente, K., Wagner, G., Lazar, M., Lange, U., Doering, Th., Rao, K.V., Zehnder, Th., Luck, I., and Lewerenz, K.-J. (1998) Thin films of semiconducting ZnS–$CuInS_2$ alloys, their characterization and use for solar cells. In: Tomlinson, R.D., Hill, A.E., Pilkington, R.D. (Eds.), Ternary and Multinary Compounds: Proceedings, ICTMC-11, University of Salford, 8–12 September, 1997, Institute of Physics Conference Series Volume, 152. CRC Press, p. 935-938.

Bonazzi, P., Bindi, L., Bernardini, G.P., and Menchetti, S. (2003) A model for the mechanism of incorporation of Cu, Fe and Zn in the stannite – kësterite series, Cu_2FeSn_4 – Cu_2ZnSnS_4. Canadian Mineralogist, 41, 639-647.

Ciobanu, C.L., Cook, N.J., Utsunomiya, S., Pring, A., and Green, L. (2011) Focussed ion beam - transmission electron microscopy applications in ore mineralogy: bridging micron- and nanoscale observations. Ore Geology Reviews, 42, 6-31.

Ciobanu, C.L., Cook, N.J., Maunders, C., Wade, B.P., and Ehrig, K. (2016) Focused Ion Beam and Advanced Electron Microscopy for Minerals: Insights and Outlook from Bismuth Sulphosalts. Minerals, 6, 112; doi:10.3390/min6040112.

Ciobanu, C.L., Maunders, C., Cook, N.J., and Wade, B.P. (2016b) Nanoscale characterization of compositionally-zoned sphalerite. Abstract, European Mineralogical Congress, Rimini, Italy, September 2016.

Cook, N.J., Ciobanu, C.L., Pring, A., Skinner, W., Shimizu, M., Danyushevsky, L., and Melcher, F. (2009) Trace and minor elements in sphalerite: A LA-ICPMS study. Geochimica et Cosmochimica Acta, 73, 4761-4791.

Cook, N.J., Ciobanu, C.L., and Williams, T. (2011a) The mineralogy and mineral chemistry of indium in sulphide deposits and implications for mineral processing. Hydrometallurgy, 108, 226-228.

Cook, N.J., Sundblad, K., Valkama, M., Nygård, R., Ciobanu, C.L., and Danyushevsky, L. (2011b) Indium mineralisation in A-type granites in southeastern Finland: insights into mineralogy and partitioning between coexisting minerals. Chemical Geology, 284, 62-73.

Cook, N.J., Ciobanu, C.L., Brugger, J., Etschmann, B., Howard, D.L., de Jonge, M.D., and Paterson, D. (2012) Determination of the oxidation state of Cu in substituted Cu-In-Fe-bearing sphalerite via µ-XANES spectroscopy. American Mineralogist, 97, 476-479.

Cook, N.J., Etschmann, B., Ciobanu, C.L., Howard, D., Williams, T., Rae, N., Pring, A., Geraki, K., Chen, G.R., and Brugger, J. (2015) Synchrotron XANES study of a Ge-(Fe)-bearing sphalerite. Minerals, 5, 117-132.

Evstigneeva, T.L., and Kabalov, Yu.K. (2001) Crystal structure of the cubic modification of Cu_2FeSnS_4. Crystallography Reports, 46, 368-372.

Evstigneeva, T.L., Rusakv, V.S., Burkovsky, I.A., and Kabalov, Yu.K. (2001) New data on the isomorphism Cu-Fe in sulphides of stannite family. In: Mineral Deposits at the Beginning of the 21st Century (A. Piestrzyñski et al., eds.), Balkema, p. 1075-1078

Fleet, M.E. (1977) Structural transformations in natural ZnS. American Mineralogist, 62, 540–546.

Frenzel, M., Hirsch, T., and Gutzmer, J. (2016) Gallium, germanium, indium, and other trace and minor elements in sphalerite as a function of deposit type—A meta-analysis. Ore Geology Reviews, 76, 52-78.

George, L.L., Cook, N.J., and Ciobanu, C.L. (2016) Partitioning of trace elements in co-crystallized sphalerite–galena–chalcopyrite hydrothermal ores. Ore Geology Reviews, 77, 97-116.

Greaney, A.T., Rudnick, R.L., Helz, R.T., Gaschnig, R.M., Piccoli, P.M., and Ash, R.D. (2017) The behavior of chalcophile elements during magmatic differentiation as observed in Kilauea Iki lava lake, Hawaii. Geochimica et Cosmochimica Acta 210, 71-96.

Hall, S.R., Szymanski, J.T., and Stewart, J.M. (1978). Kesterite, $Cu_2(Zn,Fe)SnS_4$, and stannite, $Cu_2(Fe,Zn)SnS_4$, structurally similar but distinct minerals. Canadian Mineralogist, 16, 131-137.

Kato, A. (1965) Sakuraiite, a new mineral. Chigaku Kenkyu (Earth Science Studies), 1-7 (in Japanese).

Kissin, S.A. (1989) A reinvestigation of the stannite (Cu_2FeSnS_4) - kesterite (Cu_2ZnSnS_4) pseudobinary system. The Canadian Mineralogist, 27, 689-697.

Kissin, S.A. and Owens, D.R. (1979) New data on stannite and related tin sulfide minerals. The Canadian Mineralogist, 17, 125-135.

Kissin, S.A., and Owens, D.R. (1986) The crystallography of sakuraiite. The Canadian Mineralogist 24, 679-683.

Kissin, S.A., and Owens, D.R. (1989) The relatives of stannite in the light of new data. The Canadian Mineralogist, 27, 673-688.

Liu, Q., Zhao, Z., Lin, Y., Guo, P., Li, S., Pan, D., and Ji, X. (2011) Alloyed $(ZnS)_x(Cu_2SnS_3)_{1-x}$ and $(CuInS_2)_x(Cu_2SnS_3)_{1-x}$ nanocrystals with arbitrary composition and broad tunable band gaps. Chemical Communications, 47, 964-966.

Márquez-Zavalía, M.F., Galliski, M.Á., Drábek, M., Vymazalová, A., Watanabe, Y., Murakami, H., and Bernhardt, H.-J. (2014) Ishiharaite, (Cu,Ga,Fe,In,Zn)S, a new mineral from the Capillitas Mine, Northwestern Argentina. Canadian Mineralogist, 52, 969-980.

Meisser, N., Thelin, P., Chiappero, P.-J., and Maurel, C. (1999) Laforetite, $AgInS_2$, a new mineral of the chalcopyrite group from the Montogros Mine, Haute-Loire, France. European Journal of Mineralogy, 11, 891-897.

Momma, K., Ritsuro, M., Matsubara, S., Shigeoka, M., Nagase, T., Kamada, S., Ozawa, S., Ohtani, E., Shimizu, M., and Kato, K. (2017) The crystal chemistry of sakuraiite. Acta Crystallographica Section A: Foundations and Advances, 73(a2), C910-C910.

Nitta, E., Kimata, M., Hoshino, M., Echigo, T., Hamasaki, S., Nishida, N., Shimizu, M., and Akasak, T. (2008) Crystal chemistry of ZnS minerals formed as high-temperature volcanic sublimates: matraite identical with sphalerite. Journal of Mineralogical and Petrological Sciences, 103, 145-151.

Ondruš, P., Veselovský, F., Gabašova, A., Hloušek, J., Šrein, V., Vavřín, I., Skála, R., Sejkora, J., and Drábek. M. (2003) Primary minerals of the Jáchymov ore district. Journal of the Czech Geological Society, 48, 19-147.

Pósfai, M., and Buseck, P.R. (1997) Modular structures in sulfides: sphalerite/wurtzite-, pyrite/marcasite-, and pyrrhotite-type minerals. EMU Notes in Mineralogy, 1, 193-235.

Pósfai, M., Dódony, I., and Soós, M. (1988) Stacking disorder in the ZnS from Gyöngyösoroszi, Hungary. Neues Jahrbuch für Mineralogie Monatshefte, 438-445.

Pósfai, M., Sharp, T.G., and Kontny, A. (2000) Pyrrhotite varieties from the 9.1 km deep borehole of the KTB project. American Mineralogist 85, 1406-1415.

Powell, A.V., Vaqueiro, P., Knight, K.S., Chapon, L.C., and Sánchez, R.D (2004) Structure and magnetism in synthetic pyrrhotite Fe_7S_8: A powder neutron-diffraction study. Physical Review B, 70, 014415.

Roussak, L., Wagner, G., Schorr, S., and Bente, K. (2005) Phase relationships in the pseudobinary 2(ZnTe)–$CuInTe_2$ system. Journal of Solid State Chemistry, 178, 3476-3484.

Schorr, S., and Wagner, G. (2005) Structure and phase relations of the $Zn_{2x}(CuIn)_{1-x}S_2$ solid solution series. Journal of Alloys and Compounds, 396, 202-207.

Schorr, S., Tovar, M., Stüsser, N., and Bente, K. (2004) Investigation of structural anomaly and metal ordering in the solid solution 2ZnS-$CuInS_2$ by neutron diffraction. Physica B, 350, e411-e414.

Shimizu, M., Kato, A., and Shiozawa, T. (1986) Sakuraiite: Chemical composition and extent of (Zn,Fe)In-for-CuSn substitution. Canadian Mineralogist, 24, 405-409.

Shimizu, T., and Morishita, Y. (2012) Petrography, chemistry, and near infrared microthermometry of indium bearing sphalerite from the Toyoha polymetallic deposit, Japan. Economic Geology, 107, 723-735.

Sombuthawee, C., Bonsall, S.B., and Hummel, F.A. (1978) Phase equilibria in the systems ZnS–MnS, ZnS–CuInS, and MnS–CuInS. Journal of Solid State Chemistry, 25, 391-399.

Springer, G. (1972) The pseudobinary system Cu_2FeSnS_4 - Cu_2ZnSnS_4 and its mineralogical significance. The Canadian Mineralogist, 11, 535-541.

Šrot, V., Rečnik, A., Scheu, C., Šturm, S., and Mirtič, B. (2003) Stacking faults and twin boundaries in sphalerite crystals from the Trepča mines in Kosovo. American Mineralogist, 88, 1809-1816.

Su, D.S., Neumann, W., Hunger, R., Schubert-Bischoff, P., Giersig, M., Lewerenz, H.J., Scheer, R., and Zeitler, E. (1998) Cu-Au-type ordering in epitaxial $CuInS_2$ films. Applied Physics Letters, 73, 785-787.

Wagner, G., Lange, U., Bente, K., Lenzner, J., and Lorenz, M. (2000a) Structural properties of thin $Zn_{0.62}Cu_{0.19}In_{0.19}S$ alloy films grown on Si(111) substrates by pulsed laser deposition. Thin Solid Films, 358, 80-85.

Wagner, G., Oppermann, D., Schmitz, W., Bente, K., Lenzner, J., and Lorenz, M. (2000b) Defect structure of heteroepitaxial $Zn_{2-2x}Cu_xIn_xS_2$ layers grown by pulsed laser deposition on (111) Si, (001) Si and (001) GaP substrates. Japanese Journal of Applied Physics, 39 (Suppl.), 210-215.

Wei, S.H., Ferreira, L.G., and Zunger, A. (1992) First-principles calculation of the order-disorder transition in chalcopyrite semiconductors. Physical Review B, 45, 2533-2536.

Werner, T.T., Mudd, G.M., and Jowitt, S.M. (2017) The world's by-product and critical metal resources part III: A global assessment of indium. Ore Geology Reviews, 86, 939-956.

Xu, J., Cook, N.J., Ciobanu, C.L., Li, X.F., Kontonikas-Charos, A., Gilbert, S., and Lv, Y. (2020) Indium distribution in sphalerite from sulfide-oxide-silicate skarn assemblages: a case study of the Dulong Zn-Sn-In deposit, Southwest China. Mineralium Deposita, https://doi.org/10.1007/s00126-020-00972-y

Figure captions

Figure 1. BSE (a-d) and reflected light (e) images showing sphalerite inclusions in pyrrhotite and the location of FIB cuts (foils #1-5). (a, b) Irregular In-rich sphalerite (In-Sp) inclusions in pyrrhotite (Po). (c, d) Bleb In-Sp along trails in Po. (e) Lobate sphalerite (Sp) intergrown with Po and chalcopyrite (Cp). Note inclusions of Cp of variable size in Sp and euhedral platelet of Po. Qz−quartz.

Figure 2. HAADF STEM images showing details of In-rich sphalerite (Sp). (a) Irregular sphalerite (Sp) inclusion (Foil #1) displaying In-rich and -poor domains with scalloped mutual boundaries. Note chalcopyrite (Cp) in sphalerite hosts a nanoparticle (NP) of native copper (Cu). (b) Bleb-like Sp inclusion with In-rich ZnS showing concave boundary (Foil #3). (c) Coarser ZnS inclusion in pyrrhotite (Po) crosscut by phyllosilicates (phlogopite+chlorite; Phl/Chl). Note native copper and native Bi-NPs within ZnS (Foil #2). (d) Trails of Cp NPs within lobate Sp (Foil #5). (e) Indium-rich ZnS at the boundary to pyrrhotite (inclusion shown in (c). (f) Basket-weave texture (arrowed) in In-rich ZnS from bleb in (b). (g) Detail of In-rich ZnS margin displaying scalloped/irregular and sharp morphology towards Sp and Po, respectively (Foil #1). (h) Scalloped boundary between In-rich ZnS in Sp around a native bismuth NP (Foil #2). (i) Euhedral In-Cu-rich ZnS inclusions in Sp (Foil #1). (j) Sub-rounded chalcopyrite inclusion along trails in sphalerite (Foil #5). (k) Margins between sphalerite and pyrrhotite marked by enrichment in Bi and Ag and by formation of discrete NPs of Ag-Bi-bearing minerals, possibly sulfosalts (Ag-Bi-ss; Foil #5).

Figure 3. STEM EDS maps for selected elements (as labelled) for one of the largest, irregular sphalerite inclusions displaying In enrichment (Foil #1). (a) shows composite maps (In-Zn-Cu) giving an overview of the detailed areas shown in (b)-(e). Note the obvious correlation between Cu and In distribution in ZnS (b-d). Cp−chalcopyrite; Sp−sphalerite; Po−pyrrhotite. Circles and # numbers correspond to EDS-STEM spectra in Supplemental[1] Fig. S4.

Figure 4. STEM EDS maps for selected elements (as labelled) showing In-enrichment in one of the coarser, bleb-like sphalerite (Sp) inclusions with marginal corrosion and displacement relative to a lamellae of phlogopite/chlorite (Phl/Chl) (Foil #2). (a) shows a composite map (Si-Fe-Cu-In-Zn) giving an overview of the detailed areas with In-enrichment shown in (b) and (c). Note In-enrichment around native bismuth NPs in (b)

and the Cu-, In-rich margin between sphalerite and pyrrhotite (Po) in (c). Circles and # numbers correspond to EDS-STEM spectra in Supplemental[1] Fig. S4.

Figure 5. HAADF STEM images (right) and STEM EDS maps for selected elements (as labelled) for the smallest sphalerite (Sp) blebs (a; Foil #3) and the larger, lobate sphalerite with chalcopyrite (Cp) inclusions (b; Foil #5). In (a), note the basket-weave texture for the In-rich domain (arrowed). In (b), In-richer margins are present at the contacts between chalcopyrite and host, In-bearing sphalerite. Green arrows show Ag-bearing NPs. Circles and # numbers correspond to EDS-STEM spectra in Supplemental[1] Fig. S4.

Figure 6. Plot showing compositional variation among the analyzed phases in the system ZnS-$CuInS_2$. Lattice parameters are from Wagner et al. (2000a). ZCIS[1]: intermediate compound $Zn_{2-2x}Cu_xIn_xS_2$ ($0.78<x<1$) plotted for $x=0.78$ (from Wagner et al. 2000b).

Figure 7. From left to right, FFT patterns, HAADF STEM images, simulations and structural models for sphalerite viewed on (a) [100], (b) $[01\bar{1}]$, (c) $[1\bar{1}1]$, and (d) $[1\bar{2}1]$ zone axes. The main structural motifs are marked as overlays on the images, simulations and crystal models.

Figure 8. High-resolution HAADF STEM images showing details of sphalerite (Sp); (a-b) Specimen tilted on $[0\bar{1}1]_{ZnS3C}$ and (c-e) $[100]_{ZnS3C}$. (a) Stepwise, stacking fault defects along {111} directions in ZnS_{3C} (b) Continuous boundary between In-poor and -rich domains (dashed line; Foil #1). Note that lattice distortions (dotted line) can be locally observed in the latter. (c) In-depleted Sp lamella from the basket-weave texture in In-rich Sp (Foil #3) Note structural continuity across the In-rich matrix. (d) Sharp contact between native bismuth and In-rich Sp in Foil #2. (e) Detail of (d) showing alternating bright and less-bright atoms with ½ *b* x ½ *c* periodicity. This is different from $ZnS_{[100]}$ showing atoms of equal HAADF intensity (compare with Figure 7a).

Figure 9. High-resolution HAADF STEM images showing defects in sphalerite (Sp); (a-g) specimen tilted on $[0\bar{1}1]_{ZnS3C}$, and (h, i) on $[1\bar{1}1]_{ZnS3C}$. (a, b) Stacking fault defects along conjugate {111} directions (arrowed) occurring close to areas of In-enrichment such as those shown in Figure 3d (Foil #1). (c) FFT pattern corresponding to Sp with such conjugate {111} defects. Arrows show streaking along defect directions. (d-f) Image cropped from (a) and (b) showing atom displacements along the defect highlighted as red and yellow circles. Atom arrangements change along the stacking faults from simple kinks in (d) to several dumbbell arrays

in (e, f). (g) Screw dislocations along {111} fault planes (dashed lines) display atomic disorder. (h). Structural disorder is also observed as local defects of darker intensity (arrowed). (i) Image cropped from (h) showing the decrease in total signal intensity and the disappearance of atoms along {220}, suggesting the presence of metal vacancies.

Figure 10. High-resolution HAADF STEM images showing crystal structural modifications across boundaries of In-enrichment in ZnS. (a) Transformation from [100]-cubic ZnS to [100]-tetragonal roquesite-type along 10-20 nm-wide stripes at the In-enriched boundary between sphalerite and pyrrhotite (Foil #2). (b) Preservation of the [100] cubic ZnS structure across boundaries of In-enrichment associated with quasi-regular ordering of brighter and larger atoms as a ~5Å x 5Å pattern easy to visualize at the direct contact (dashed line) with ZnS. FFT pattern (inset) shows the lattice with quasi-ordering of brighter atoms within the ZnS substructure. (c) Image cropped from (a) showing the roquesite-type pattern with a dumbbell atomic arrangement on [100] as shown in STEM simulation in the inset. (d) FFT pattern corresponding to (c) with satellite reflections at ½ <011>* (yellow circles; T=tetrahedral). (e) Image cropped from (b) showing an area with more ordered distribution of brighter atoms attributable to columns of In-(Cu, Zn) mixed sites (yellow circles). (f) FFT pattern corresponding to image in (e) displaying satellite reflections (yellow circles) along $b*$ and $c*$ forbidden in the space group $F\bar{4}3m$ of ZnS_{3C} (arrowed). The pattern and FFT are distinct from the roquesite-type structure (Supplemental[1] Fig. S4) and correspond to ZnS with $P\bar{4}3m$ symmetry (see Figure 12 for interpretation).

Figure 11. Plot of (Fe+Cu+Ag+In+Sn+Ga) a.p.f.u. vs. Zn a.p.f.u. for In-rich ZnS from Dulong and other localities. [1]Capillitas Mine, Argentina (Marquez-Zavalia et al. 2014); [2]Ikuno Mine, Japan) (Kissin and Owens 1986); [3]Toyoha, Japan (Ciobanu et al. 2011).

Figure 12. (a-c) From left to right, crystal model, SAED and STEM simulations for In-rich ZnS with $P\bar{4}3m$ symmetry and empirical formula $(Cu,In,Zn)_3(Zn_{0.5}Fe_{0.5})S_4$ modelled as a phase with two mixed sites: Me1a (In, Cu, and Zn); and Me3c (Fe, Zn). (d, e) Image and total intensity profile of In-rich ZnS along directions showing variation in signal intensity according to the considered model for In-rich ZnS. (f, g) Sphalerite image and total intensity profiles along two of the three directions shown for In-rich ZnS. Note the uniform signal intensity for Zn sites on both profiles.

Table 1. Overview of selected published data for phases in the system ZnS-$CuInS_2$ and related species

Mineral	Locality	Formula	System	Space group	a (Å)	b (Å)	c (Å)	Reference
Sphalerite Group								
Sphalerite	Jachymov, Czech Rep.	$Zn_{0.9}Fe_{0.11}S_{0.99}$	Cubic	$F\bar{4}3m$	5.4174	5.4174	5.4174	Ondruš et al. (2003)
Sphalerite	Iwodake, Japan	$Zn_{0.968}Fe_{0.023}Cu_{0.005}In_{0.002}Cd_{0.002})_1S$	Cubic	$F\bar{4}3m$	5.4159	5.4159	5.4159	Nitta et al. (2008)
Ishiharaite	Capillitas, Argentina	(Cu,Ga,Fe,In,Zn)S	Cubic	$F\bar{4}3m$	5.368	5.368	5.368	Márquez-Zavalía et al. (2014)
Related to sphalerite group								
Sakuraiite	Ikuno, Japan	$(Cu,Zn,Fe)_3(In,Sn)S_4$	Tetragonal	(not given)	5.455	5.455	10.91	Kato (1965)
Sakuraiite	Japan	$(Cu,Zn,Fe)_3(In,Sn)S_4$	Tetragonal	$P\bar{4}2m$	5.45	5.45	5.4691	Momma et al. (2017)
Sakuraiite	Ikuno, Japan	(Cu,Zn,Fe,In,Sn)S	Cubic	3 alternatives*	5.4563	5.4563	5.4563	Kissin and Owens (1986)
Chalcopyrite Group								
Chalcopyrite		$CuFeS_2$	Tetragonal	$I\bar{4}2d$	5.289	5.289	10.423	Hall and Stewart (1973)
Roquesite	Synthetic	$CuInS_2$	Tetragonal	$I\bar{4}2d$	5.52279	5.52279	11.13295	Abrahams and Bernstein (1973)
Laforetite	Montgros, France	$AgInS_2$	Tetragonal	$I\bar{4}2d$	5.88	5.88	11.21	Meisser et al. (1999)
Stannite Group								
Stannite	Oruro, Bolivia	$Cu_2(Fe,Zn)SnS_4$	Tetragonal	$I\bar{4}2m$	5.449	5.449	10.757	Hall et al. (1978)
Kësterite	Oruro, Bolivia	$Cu_2(Zn,Fe)SnS_4$	Tetragonal	$I\bar{4}$	5.427	5.427	10.8751	Hall et al. (1978)
Kësterite	Synthetic	Cu_2ZnSnS_4	Tetragonal	$I\bar{4}2m$	5.434	5.434	10.856	Bonazzi et al. (2003)
Petrukite	Multiple localities	$(Cu,Fe,Zn)_3(Sn,In)S_4$	Orthorhombic	$Pmn2_1$	7.6671	6.4399	6.2605	Kissin and Owens (1989)
Cubic Cu_2FeSnS_4	Synthetic	Cu_2FeSnS_4	Cubic	$F\bar{4}3m$	5.4179	5.4179	5.4179	Evstigneeva and Kabalov (2001)

* Three possible space groups considered: $P432$, $P\bar{4}3m$ and $Pm3m$

Table 2. STEM EDS compositional data for sphalerite grains in studied foils

	***In wt.% (measured)**			****Mol.% $CuInS_2$ (calculated)**		
	Mean	Min.	Max.	Mean	Min.	Max.
Foil #1						
Sphalerite (n=11)	0.92	0.58	1.59	1.6	1	2.7
In-rich sphalerite (n=15)	17.95	10.41	24.85	36.5	19.1	48.8
Foil #2						
Sphalerite (n=8)	0.67	0.38	1	1.2	0.7	1.7
In-rich sphalerite (n=10)	14.58	9.17	20.77	29.9	17.2	45.5
Foil #3						
Sphalerite (n=3)	1	0.66	1.54	1.8	1.1	2.8
In-rich sphalerite (n=5)	20.26	18.04	21.09	42.9	41.9	45.3
Foil #5						
Sphalerite (n=10)	0.39	0.24	0.63	0.7	0.4	1.1

*Measured Cu contains excess Cu from TEM grid thus measured In, Zn, S etc, are lower.

**Calculated assuming Cu=In (atom.% basis) and substitution 2(Zn,Fe) ↔ Cu + In, ignoring <1.0 wt.% concentrations of Ag and Sn in some analyses.

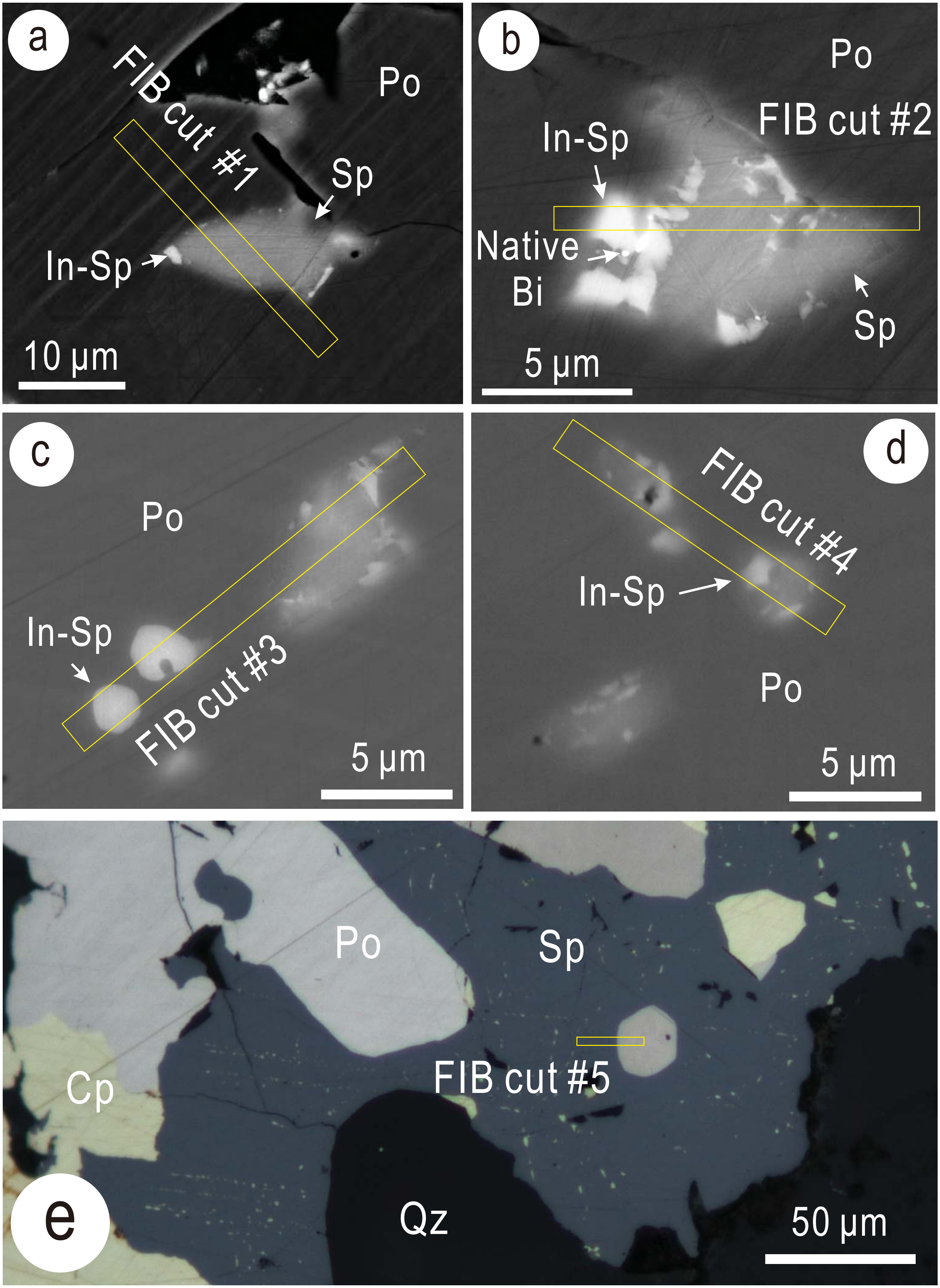

Figure 1. Xu et al.

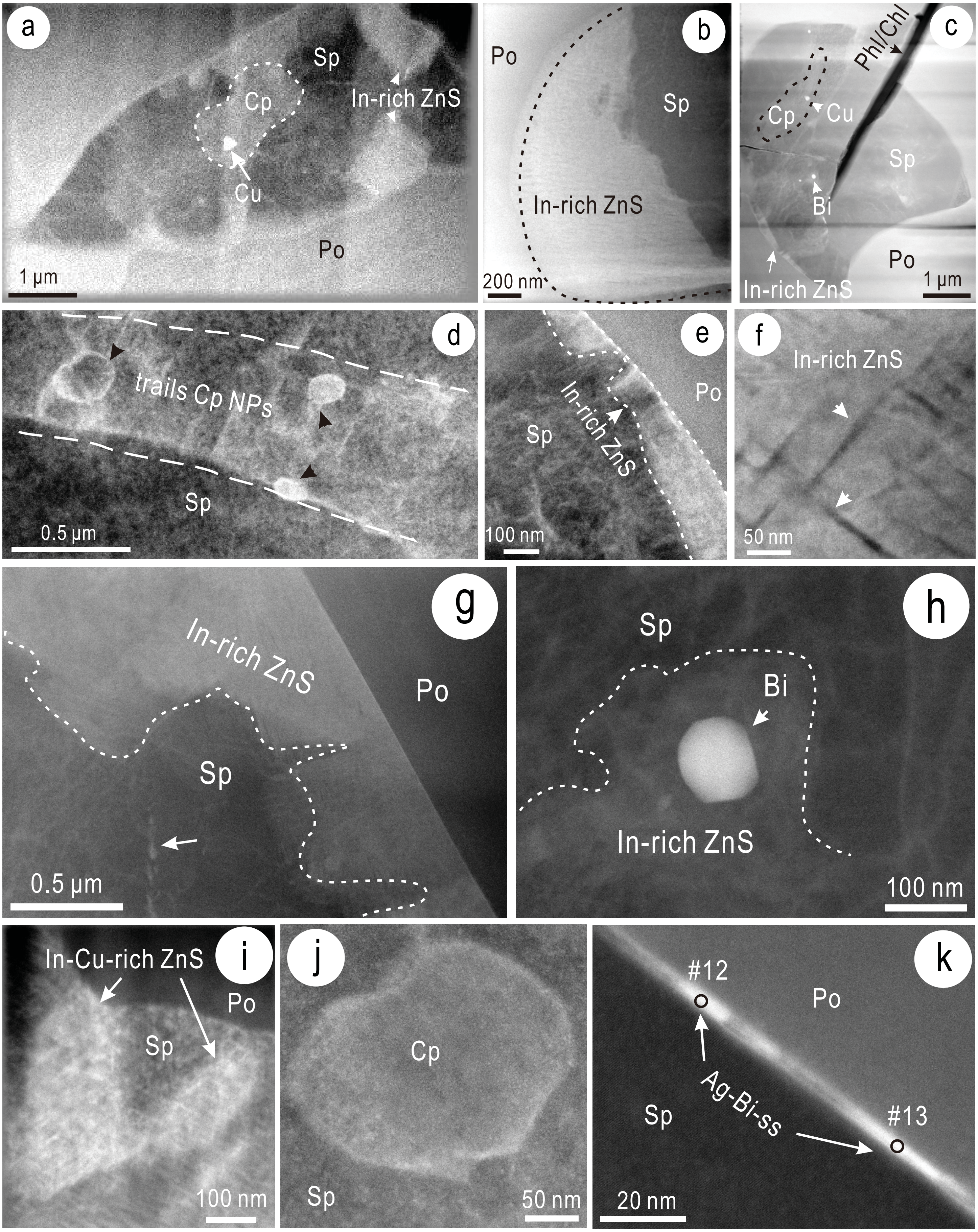

Figure 2. Xu et al.

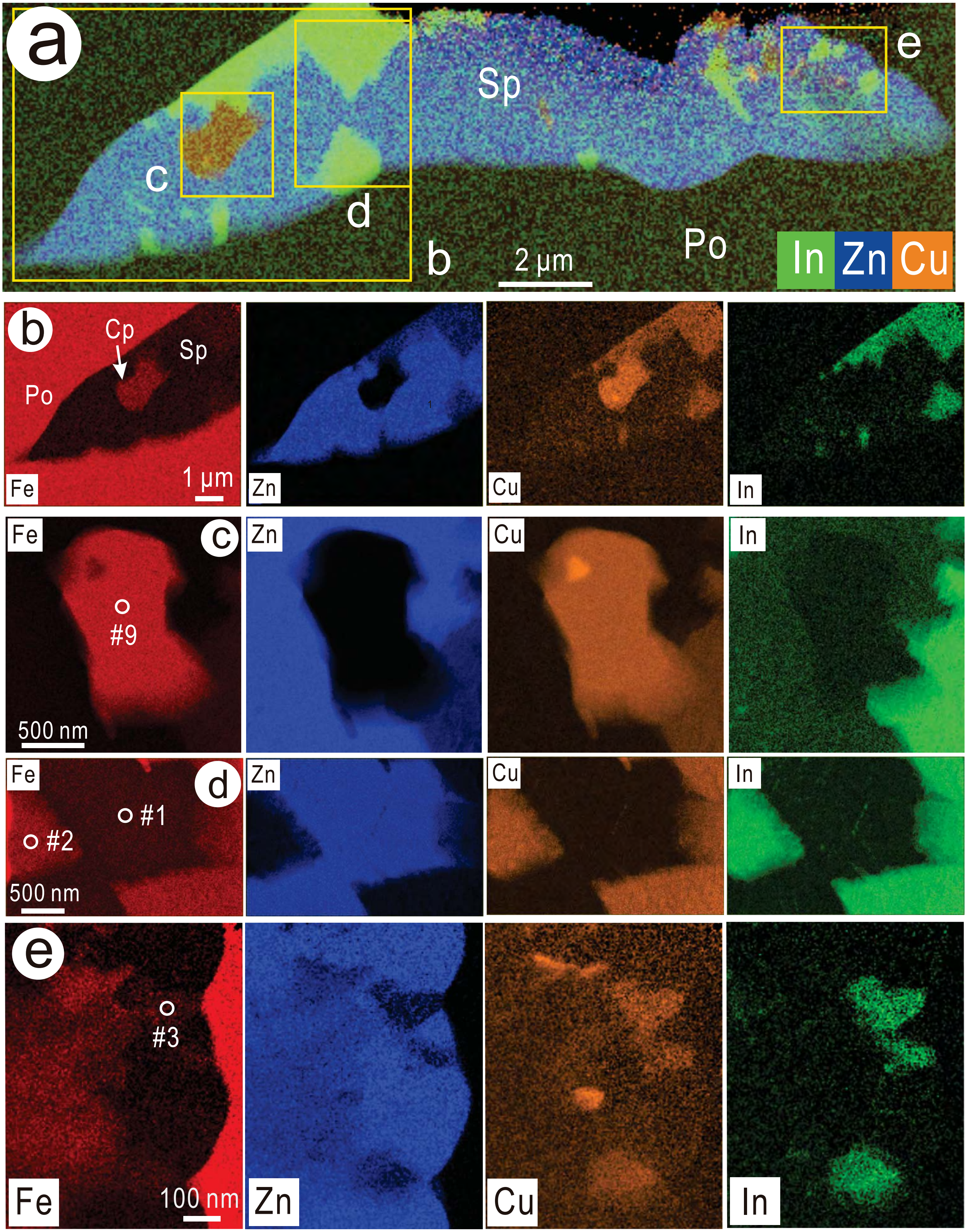

Figure 3. Xu et al.

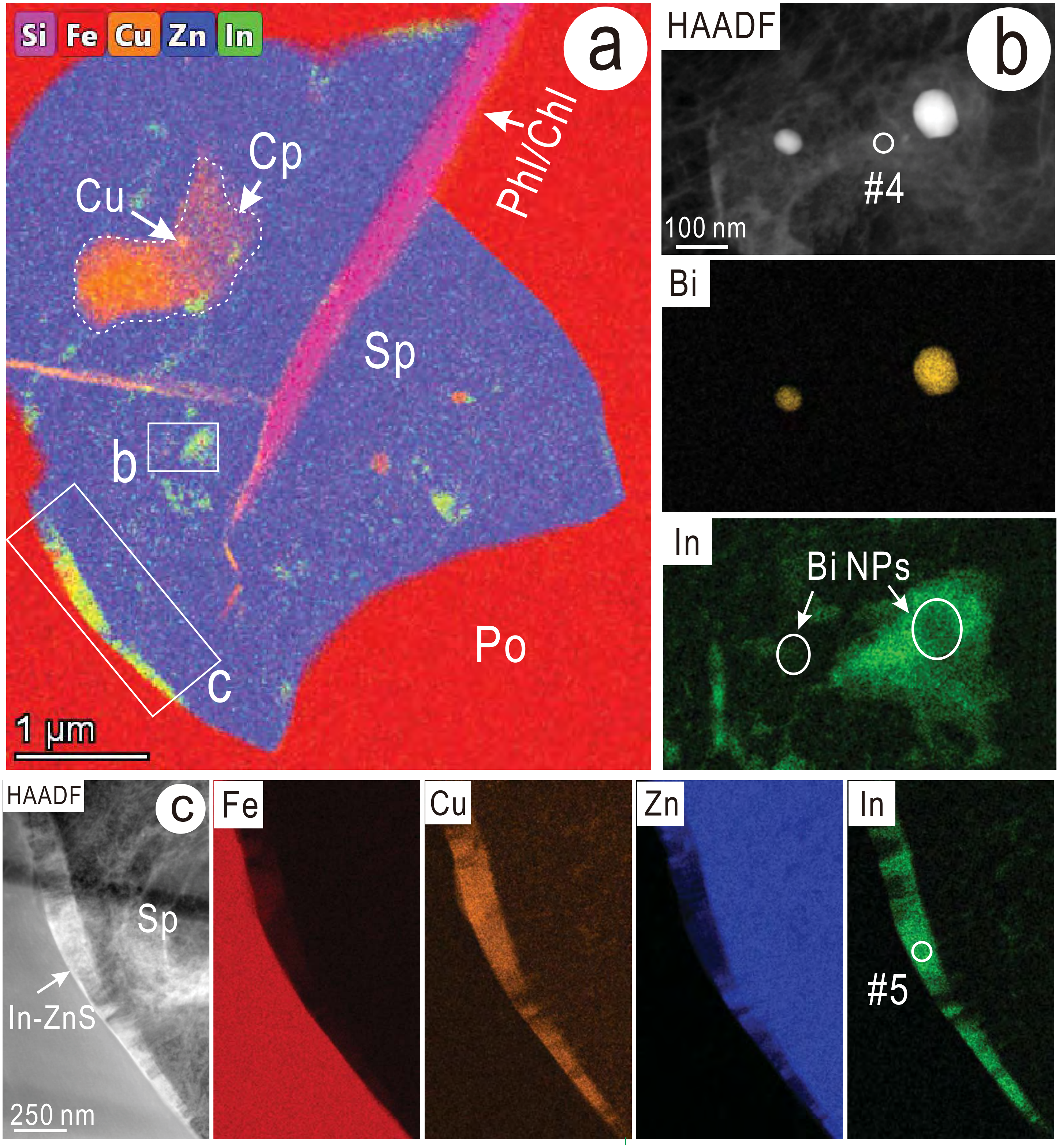

Figure 4. Xu et al.

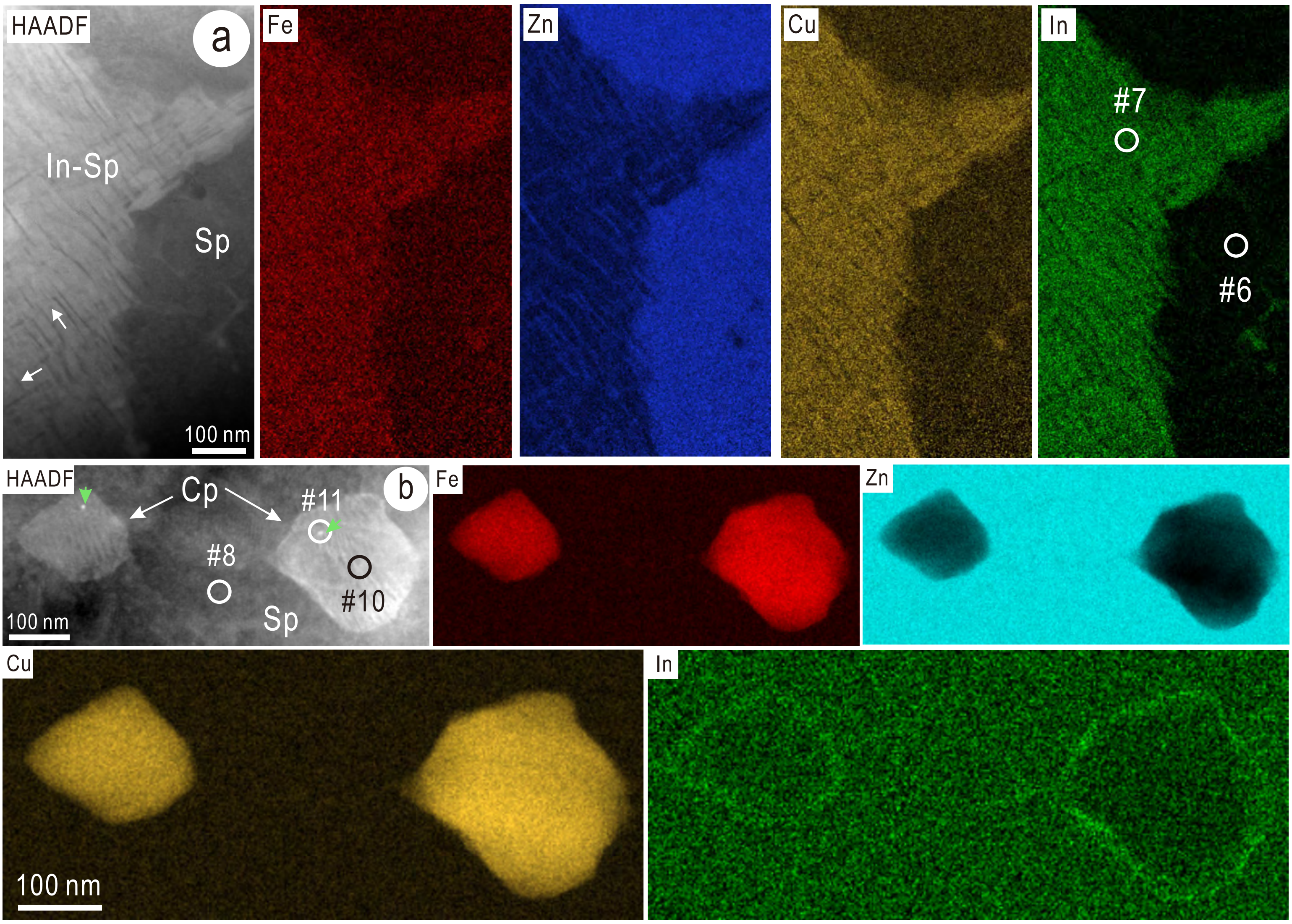

Figure 5. Xu et al.

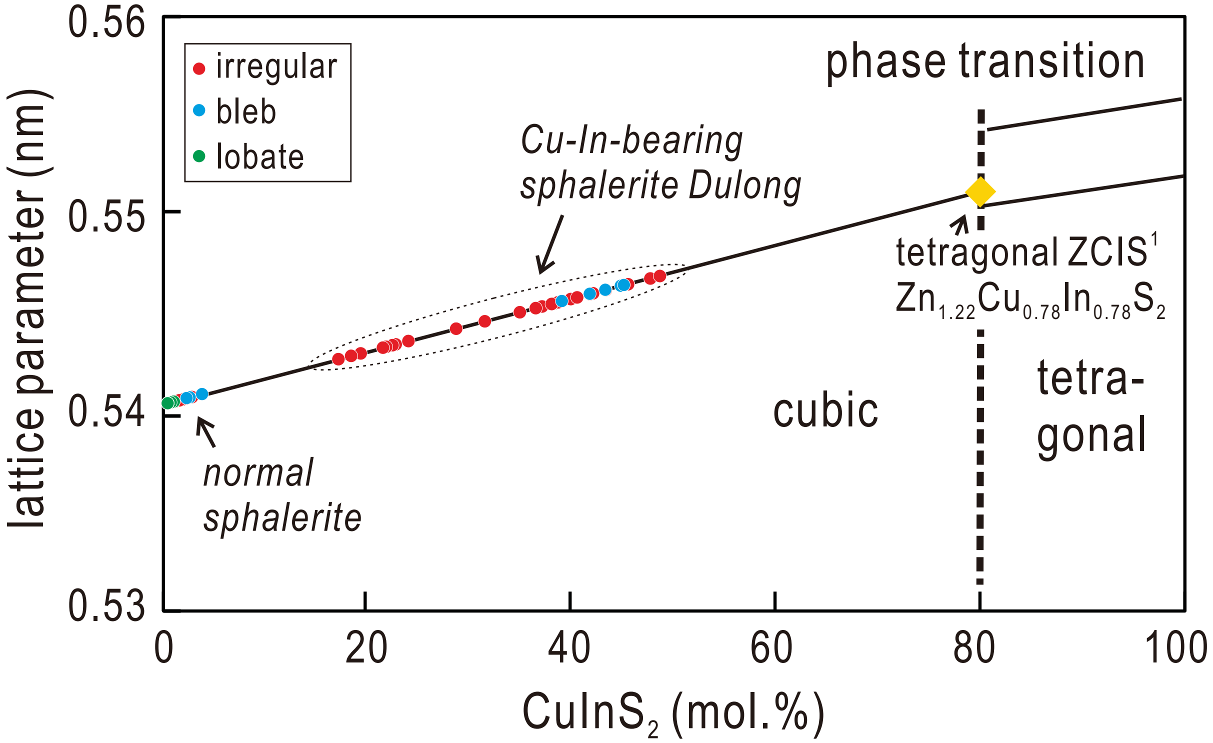

Figure 6. Xu et al.

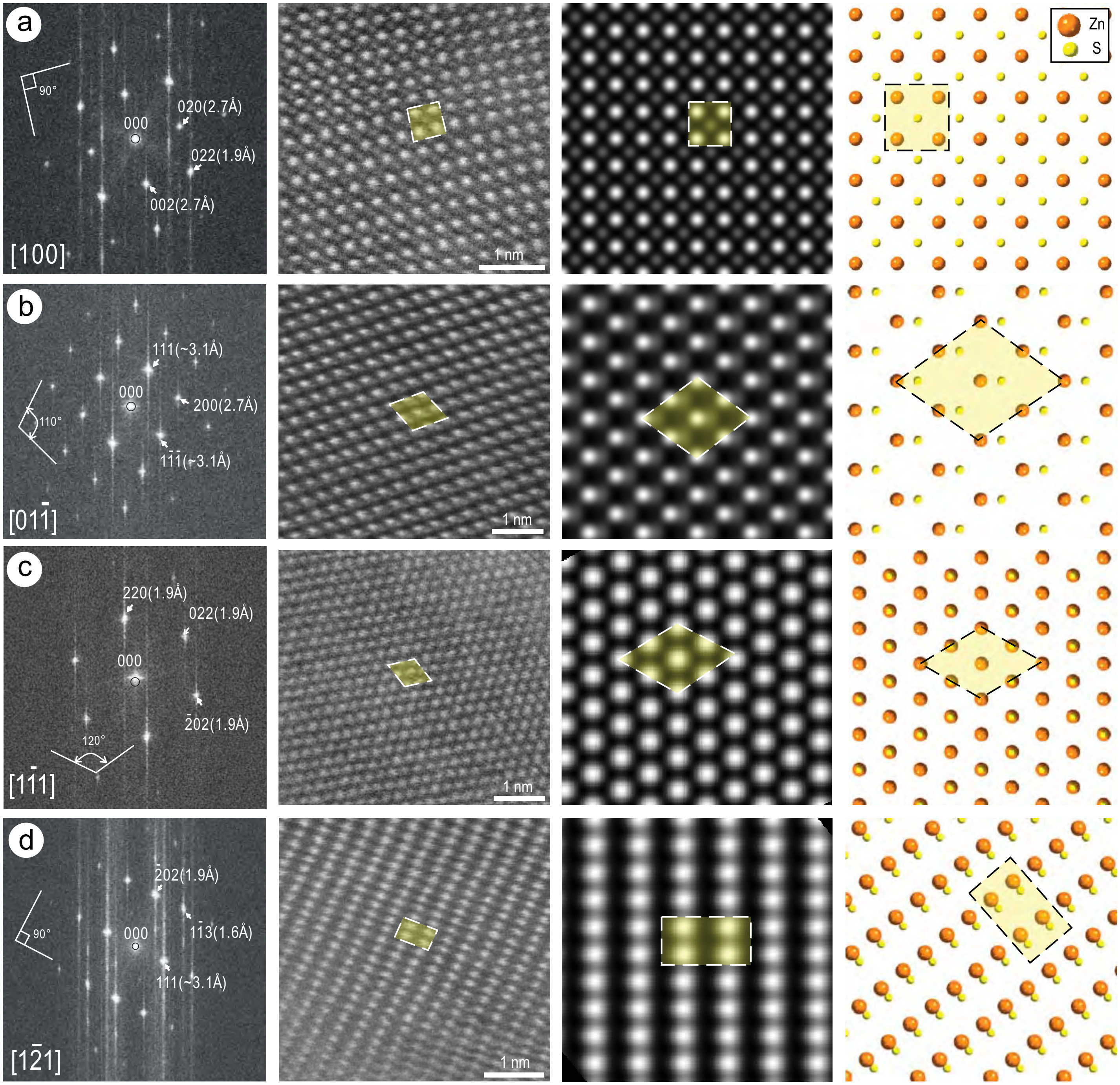

Figure 7. Xu et al.

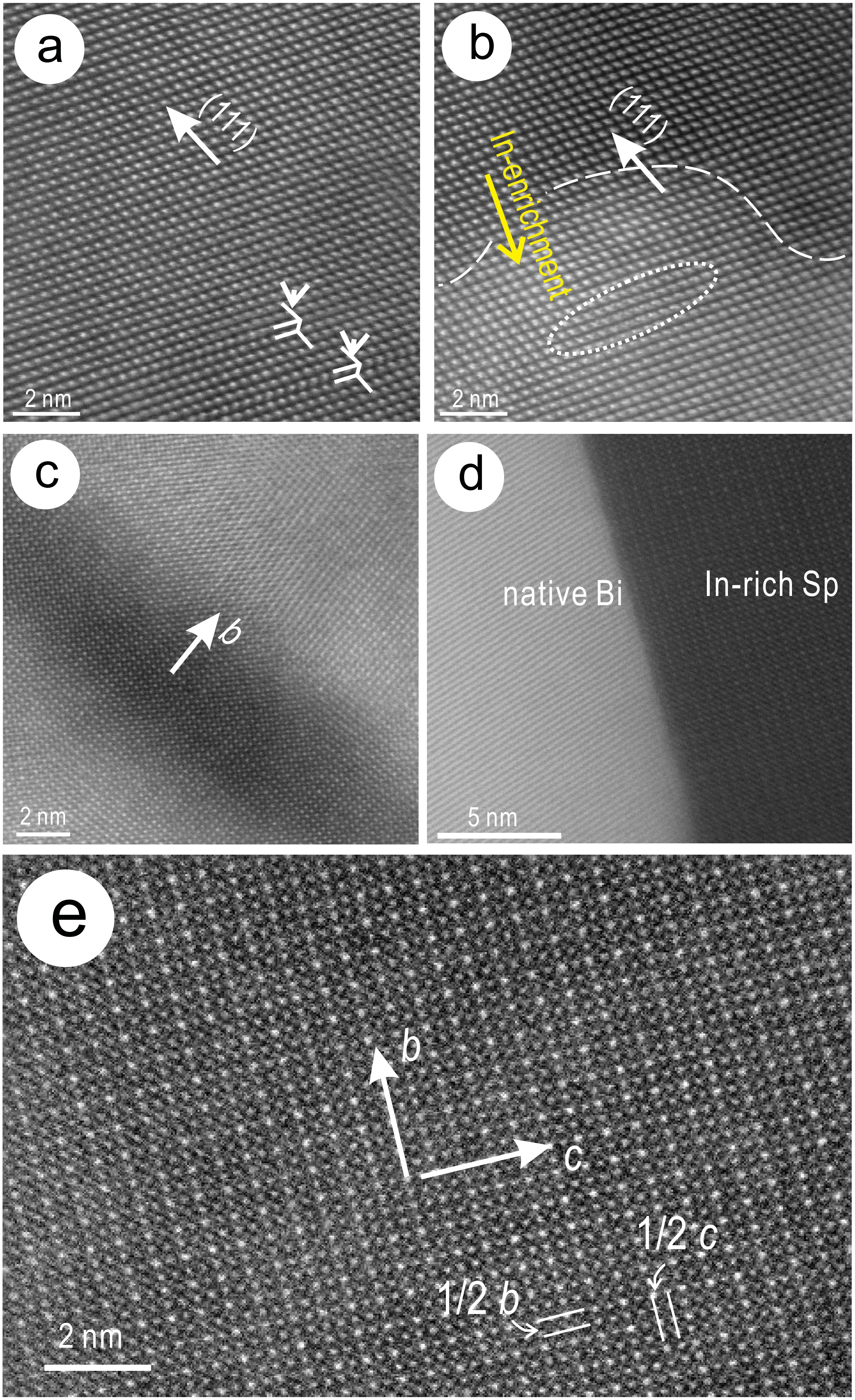

Figure 8. Xu et al.

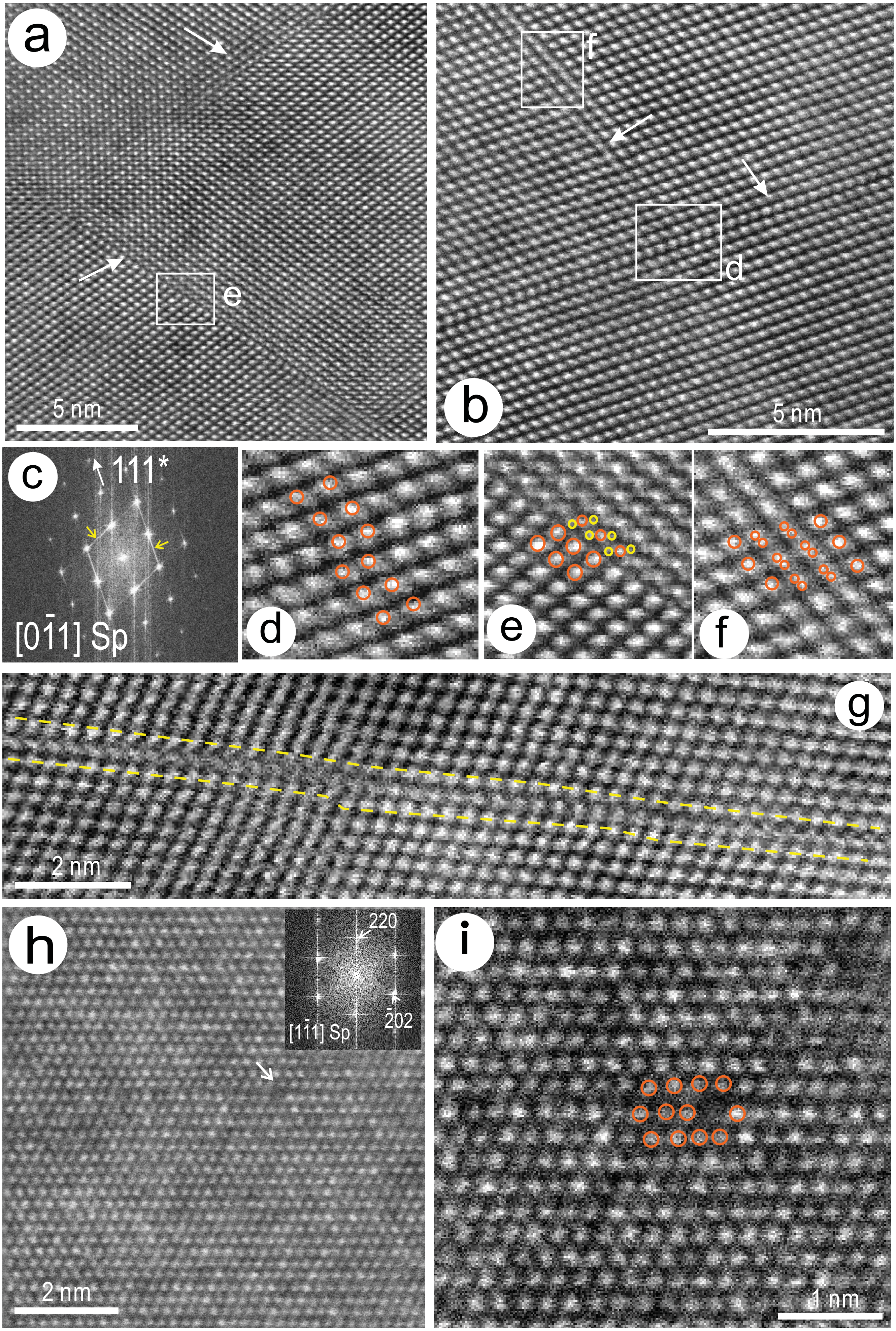

Figure 9. Xu et al.

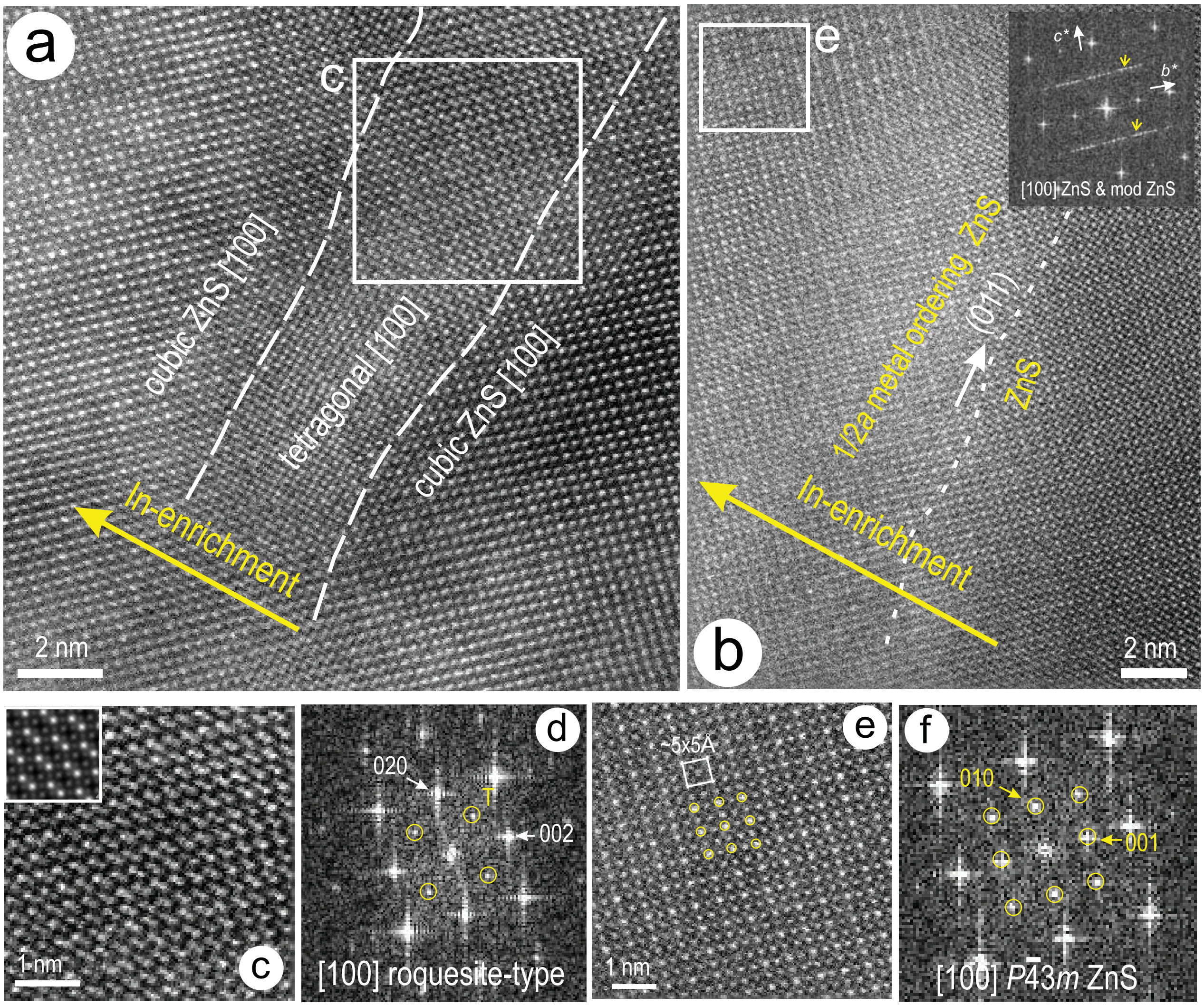

Figure 10. Xu et al.

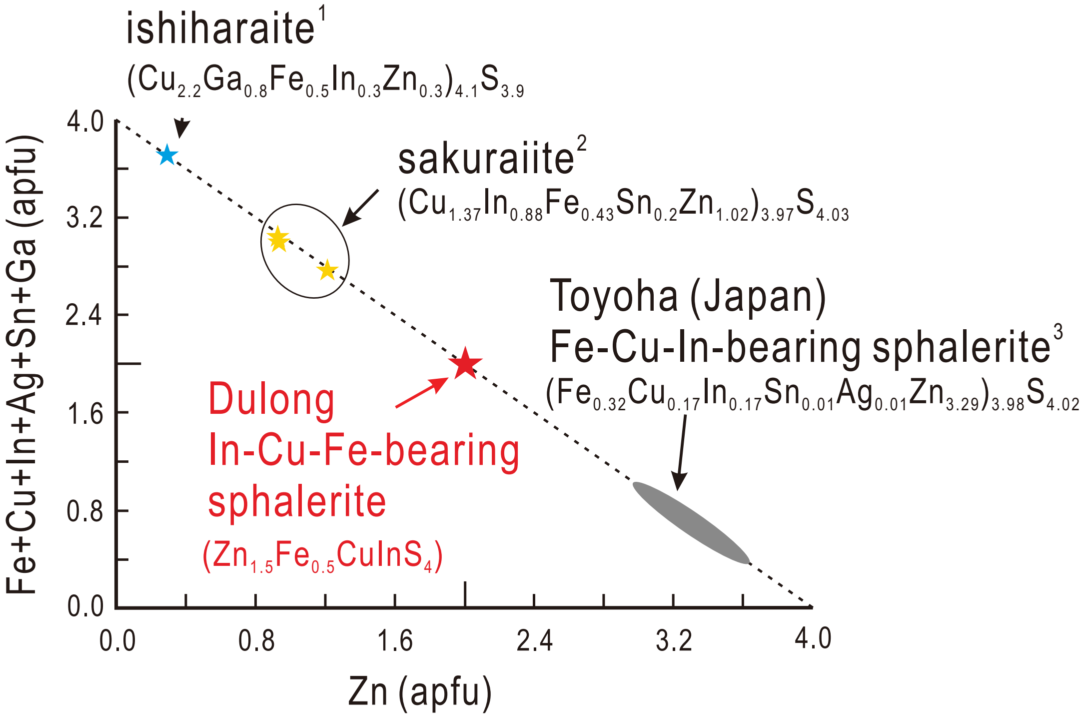

Figure 11. Xu et al.

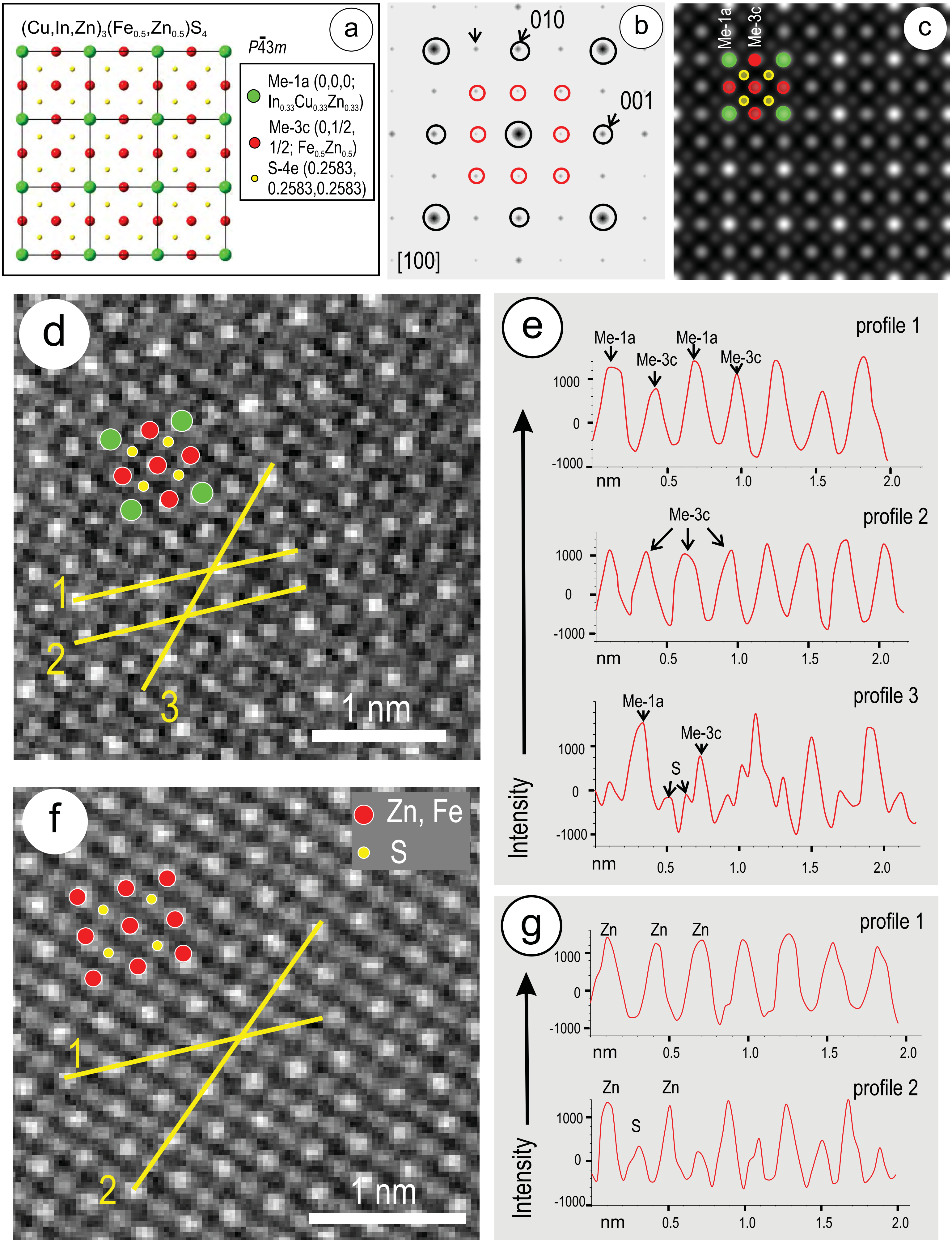

Figure 12. Xu et al.